# ISOTOPIC EFFECTS IN NUCLEAR FRAGMENTATION AND GCR TRANSPORT PROBLEMS

Francis A. Cucinotta
NASA, Johnson Space Center
Houston TX, 77058

**Abstract:**

Improving the accuracy of the galactic cosmic ray (GCR) environment and transport models is an important goal in preparing for studies of the projected risks and the efficiency of potential mitigations methods for space exploration. In this paper we consider the effects of the isotopic composition of the primary cosmic rays and the isotopic dependence of nuclear fragmentation cross sections on GCR transport models. Measurements are used to describe the isotopic composition of the GCR including their modulation throughout the solar cycle. The quantum multiple-scattering approach to nuclear fragmentation (QMSFRG) is used as the data base generator in order to accurately describe the odd-even effect in fragment production. Using the Badhwar and O'Neill GCR model, the QMSFRG model and the HZETRN transport code, the effects of the isotopic dependence of the primary GCR composition and on fragment production for transport problems is described for a complete GCR isotopic-grid. The principle finding of this study is that large errors ($\pm$ 100%) will occur in the mass-flux spectra when comparing the complete isotopic-grid (141 ions) to a reduced isotopic-grid (59 ions), however less significant errors (<30%) occur in the elemental-flux spectra. Because the full isotopic-grid is readily handled on small computer work-stations, it is recommended that they be used for future GCR studies.

## INTRODUCTION

In the description of the transport of the galactic cosmic rays (GCR) in shielding materials or tissue, a common approximation is to consider only the elemental composition of the primary GCR and a reduced isotopic-grid for the secondary nuclei produced in nuclear fragmentation interactions. In this paper, we analyze the role of the isotopic dependence of the GCR primary composition and nuclear fragmentation in predicting the flux of the GCR behind arbitrary shielding configurations. NASA has set a strategic goal of determining the GCR flux spectra to within $\pm$25% accuracy (Annon. 1998). Our study is an important milestone in achieving this goal, since for the first-time a full isotopic-grid has been achieved in a GCR transport model and we document the error inherent in former approaches. Also, for applications that will consider radioactive isotopes produced in the atmosphere or shielding, our study provides a useful tool to perform such analyses.

Historically the HZETRN code grew from a 29-isotopic grid used in the 1980's and early 1990's (Wilson, *et al.,* 1991) to an extension to 32 isotopic-grid in order to include all light ions (Cucinotta, 1993). Because of the limitations of random access memory present in the computer workstations of the early 1990's, sensitivity studies were made for mono-energetic ion beams to study the minimum number of isotopes for convergence resulting in the use of 59-isotopic grid (Kim, *et al.,* 1994), and all GCR studies since 1994 have used the 59-isotopic grid (Shinn, *et al.,* 1994). However, there are several reasons to re-consider the use of the full isotopic-grid for GCR transport problems. First, the isotopic dependence of the primary GCR has not been considered in the past and may lead to errors in the description of both primary ion attenuation and secondary particle production. Secondly, the studies of Kim *et al.* (1994) used the NUCFRG2 model of fragmentation (Wilson *et al.*, 1994), which does not provide a correct description of the even-odd effect observed in fragment production and of the projectile isospin dependence observed experimentally (Knott, *et al.,* 1996, 1997; Zeitlin *et al.,* 2001). Thirdly, the sensitivity studies made by Kim et al. 1994 used a "calibration" of the isotopic-grid to

$^{56}$Fe beams, however a larger isotopic grid occurs when all GCR projectile nuclei are considered. Fourth, the error in the range-energy and stopping powers that results from the use of a reduced isotopic grid, although expected to be small for large mass number, A>>1, is an unnecessary one for transport calculations. Finally, the improved computational speed and memory available on current small computer workstations, makes the inclusion of a full isotopic-grid in the HZETRN code to be straightforward problem at this time.

## GCR ISOTOPIC COMPOSITION

Theoretical models and upper atmosphere and satellite measurements of the GCR have long considered the isotopic composition of the GCR in order to understand the source of these particles and their modification through transport through space (Parker, 1965). Theoretical models consider the transport of the GCR through the inter-planetary medium in order to extract the primary nuclear composition at stellar sources (Parker, 1965, Webber, *et al.*, 1990a). Experimental studies have included measurements at the top of the Earth's atmosphere and on the Pioneer I and II spacecraft. A survey of such data (Hesse *et al.*, 1991; Lukasiak, *et al.,* 1993; Webber *et al.*, 1985, 1990; Wiedenback *et al*, 1981, 1985) was made with the results shown in Table I. For this compilation, we note that since secondary fragment production is modulated by the time spent in the inter-planetary medium, the isotopic fraction is dependent on position in the solar cycle. In Table I we have used data on isotopic fractions near solar maximum where the isotopic fraction for nuclei produced within the heliosphere are expected to be at a maximum (Hesse et al., 1991; Lukasiak, *et al.*, 1993; Webber, *et al.,* 1985, 1990; Wiedenback, *et al*, 1981, 1985). We then used estimates of the source abundances and the modulation parameter to estimate the isotopic fraction as a function of position in the solar cycle. Based on the results of Lukasiak *et al.* (1993), we use the following empirical formula to describe the dependence of the isotopic ratio (near-Earth) on the solar cycle as described using the modulation parameter $\phi(MV)$

(1) $f(A,Z) = f_{Source}(A,Z) + [\exp(\gamma\sqrt{\phi}) - 1]$

where $\gamma$ is found by interpolating from the source and near solar maximum values. The isotopic fraction is than scaled to the Badhwar and O'Neill model spectra (1992) for the most abundant isotope of a given charge to obtain the primary isotopic energy spectra. For the *Z=1* and *Z=2* ions we use the empirical formula of Cucinotta *et al.* (1993) to estimate the primary (near-Earth) deuteron and helion spectra. Figure 1 shows results for the empirical scaling on the solar modulation parameter described by eq.(1) for $^{13}C$ and $^{15}N$.

## ISOTOPIC EFFECTS IN GCR TRANSPORT

The Boltzmann transport equation within the straight-ahead and continuos slowing down approximations and assuming velocity conservative fragmentation events, describes the heavy ion flux, $\phi_j(E,x)$ of an ion $j$ with mass number $A_j$ and charge number $Z_j$, energy $E$ (in unites of MeV/u) at shielding depth $x$ (in units of g/cm$^2$) and is written (Wilson, *et al.* 1991)

(3) $$[\frac{\partial}{\partial x} - \frac{1}{S_j(E)}\frac{\partial}{\partial E} - \sigma_j(E)]\phi_j(x,E) = \sum_k \sigma_{j,k}(E)\phi_k(E,x)$$

where $\sigma_j(E)$ is the energy-dependent absorption cross section (cm$^{-1}$) and $\sigma_{jk}$(E) is the fragmentation cross section for producing an ion $j$ from $k$. Because eq. (3) is a coupled integro-differential equation for the many GCR primary and secondary nuclei, required memory allocations will increase rapidly as the number of ion species is increased. However, such practical limitations no longer exist on small computer workstations and an unrestricted isotopic-grid can presently be implemented with no memory or storage problems. When using a reduced isotopic grid, fragments not contained in the grid are assigned to a nearby mass of identical charge number. This introduces two types of errors: First the range-energy and stopping powers are altered from their true values. This

error is expected to be small at high-energies for A>>1 since here ion ranges are well described by $A_j/Z_j^2$ scaling factors. The second type of error occurs in the absorption and fragmentation cross sections. Here because of the re-assignment of the mass number when using a reduced grid, an error is introduced by the change in neutron number from its true values. Such errors arise from the atomic transport properties, from the isotopic-spin dependence of fragment spectra, and in the spectra of high-energy neutrons produced in fragmentation events. This latter error is expected to be small because high-energy neutrons are largely produced by light-particle (n, p, d, t, h, and $\alpha$) interactions on target nuclei especially for larger target atoms (A>10), but may be non-negligible for light target atoms (Cucinotta, *et al.* 1998a). Since materials with high-hydrogen content are known to be the optimal shielding materials, the changes in the neutron flux due to the used of a full isotopic-grid should be considered.

## QUANTUM ABRASION-ABLATION

The quantum multiple scattering description of the fragmentation (QMSFRG) has been quite successful in describing heavy ion fragmentation data (Cucinotta, *et al.* 1994, 1997, 1998b). The prior work considered the derivation of the pre-fragment excitation spectrum following nucleon or alpha particle abrasion and showed that the excitation spectrum could be represented in terms of an impact parameter dependent convolution of the pre-fragment excitation response for a transition of the pre-fragment core from state $n$ to $n'$ and the project fireball response,

$$(4) \qquad \frac{d\sigma}{d\varepsilon_{F^*}} = \langle T | \int d^2q d^2b d^2b' \; e^{iq(b-b')} P_{n,n'}(b,b') \Lambda_{n,n'}(q,b,b,E_{F^*}) | T \rangle$$

where $b$ $(b')$ is the impact parameter, and $q$ the momentum transfer. The abrasion response is defined as the interaction of the projectile fireball with the target after performing closure over the final fireball states

$$(5) \quad \Lambda_{n,n'} = \int \frac{d\mathbf{k}_R}{(2\pi)^3} < R' | Q_{RT}^{+}(b') | R >< R | Q_{RT}(b) | R' > \delta(E_i - E_f)$$

where the $Q_{RT}$ represent the fireball-target profile operator, and $k_R$ the projectile fireball momentum vector. The abrasion-response represents a complicated many-body operator. The pre-fragment excitation is described in terms of the transition matrix

$$(6) \quad P_{n,n'} = < F^*_n | Q_{F^*T}^{+}(b') | F^*_{n'} >< F^*_{n'} | Q_{F^*T}(b) | F^*_n >$$

where the matrix elements for the pre-fragment excitation are evaluated over the many-body profile operators, $Q_{FT}$. In the present model a convolution approach is used to derive the mutli-knockout spectrum using the single-fragmentation term (Cucinotta and Dubey, 1994).

The de-excitation of the pre-fragments in the QMSFRG model is described in a stochastic process using a Master equation for nuclear de-excitation by particle emission (Cucinotta *et al.*, 1997). Let $f^b(E,t)$ be the probability of finding the nuclei $b$ at time $t$ with excitation energy $E_b$ and $P_k^b(E)$ be the probability that the nuclei, $b$ will emit ion $k$ with energy $E$, then the Master equation is

$$(7) \quad \frac{df^b(E^*_b,t)}{dt} = \sum_j \int dE\, f^a(E^*_a,t) P_j^a(E) - \sum_k \int dE f^b(E^*_b,t) P_k^b(E)$$

In eq. (7) the first-term on the right corresponds to gains by decays $a$ -> $b+j$ and the second terms from losses dues to decays $b$ -> $c+k$ where the $j$ *(or k)* are light-particle emissions (*n, p, d, t, h, or* $\alpha$). Equation (7) is solved by iteration up to medium excitation energies (<150 MeV) and by approximation for high excitation energies (Cucinotta *et al.* 1997, 1998b). An important feature of the solution is the correct description of the level-density including the description of nuclear-shell effects at low-excitation energies, and the use of measured values for the nuclear masses. The fragmentation cross section is then evaluated from equations (4)-(7) as

$$(8)\quad \sigma_F(A_F, Z_F) = \sum_{A_F^*, Z_F^*} \int dE_{F^*} \frac{d\sigma_{F^*}}{dE_{F^*}} f(A_{F^*}, Z_{F^*} \longrightarrow A_F, Z_F)$$

where $f(A_{F^*}, Z_{F^*} \longrightarrow A_F, Z_F)$ is the solution to equation (7).

The QMSFRG theory reduces to the OPTFRG model (Townsend *et al.*, 1986) when energy conservation is ignored and the closure approximations on the pre-fragment and fireball states are made, and to the NUCFRG2 model (Wilson, *et al.* 1995) when the optical operators are expressed as volume overlaps functions. In both the OPTFRG and NUCFRG2 models all information on the pre-fragment excitation spectrum is lost and thus must be introduced in an *ad-hoc* manner independent of the collision model used to describe mass removal.

## RESULTS AND DISCUSSION

We first illustrate the accuracy of the QMSFRG model and the effects of isospin on fragmentation cross sections. Figures 2-9 show comparisons of the model to experimental data for the elemental distributions of fragments for several nuclei of similar mass number. The isospin, $T_z=0$ nuclei display large odd-even effects, which are reduced for the $T_z \neq 0$ nuclei. The odd-even effects are present for all target nuclei, however are reduced for hydrogen targets due to the small abrasion probability for large mass removal on hydrogen. One of the errors that can be seen in transporting ions using a reduced mass-grid by comparing fragmentation cross sections for nearby projectiles where large differences in many of the production cross sections occur for neighboring projectile nuclei. The model accurately reproduces the effects observed in the experiments. Figures 10 and 11 show comparison of QMSFRG results to experiments for the isotopic distribution of fragments for $^{40}$Ar and $^{56}$Fe projectiles. The results show good agreement between theory and experiments and indicate the larger number of isotopes that are produced during nuclear fragmentation.

Figure 12 shows results from the HZETRN code at solar minimum ($\phi$=*428 MV*) behind 5 g/cm$^2$ of aluminum shielding. Comparison of the mass-flux spectra for a 59-isotope grid and the full 141-isotope grid are shown. The 141-isotope grid was developed by considering the fragmentation cross sections for a large number of GCR primary nuclei and dominant fragments in several materials. In Figure 12 we have scaled the flux by the charge-squared of the ion as a measure of the ionization power of each mass group. Large differences are seen for many nuclei, especially odd-mass nuclei and the non-abundant even-mass nuclei. Figure 13 shows the percent error resulting from the use of the reduced isotopic-grid for shielding depths of 5 and 20 g/cm$^2$ of aluminum. Errors greater than 100% are seen for many nuclei, however in most cases such large errors only occur for the less abundant nuclei. Biological effects are expected to be approximately proportional to $Z^2$ and the elemental-flux distribution may be a sufficient test of transport models for supporting exploration studies. In Figure 14 we show a similar comparison to that of Figure 13, however here for the elemental-flux distribution. The errors are indeed less substantial than those of the mass-flux distribution, yet are larger than 10% in many cases. Similar comparisons are near solar maximum conditions ($\phi$=*1000 MV*) are shown in Figures 15 and 16. The errors at solar maximum are slightly larger than at solar minimum because of the larger buildup of "secondary" nuclei in the heliosphere for these conditions.

A major part of developing the description of GCR transport are theoretical models and experimental data on the nuclear interactions and propagation of heavy ions (Z>2). Over the last 30 years such descriptions have improved dramatically with the development of an accurate free space GCR model (Badhwar and O'Neill, 1992), the HZETRN code (Wilson, et al., 1990), the measurement of a significant number of fragmentation cross sections (for e.g., Brechtmann and Heinrech, 1988; Knott, *et al.* 1996, 1997; and Zeitlin *et al.,* 1997, 2001, 2002), and the development of an accurate nuclear fragmentation model (Cucinotta *et al.,* 1998a). Laboratory (Shimmerling, *et al,* 1989), and spaceflight (Badhwar and Cucinotta, 2000) validation data have also become available during this time period. The implementation of heavy transport models has progressed from models

that lacked unitarity (Letaw, *et al.* 1983) to the current fully energy-dependent models with accurate absorption cross sections (Shinn, *et al.* 1994; Wilson, *et al.*, 1993; Cucinotta, 1993). Future work may still be required for light-particle transport (*n, p, d, t, h,* $\alpha$, and mesons and their decays), including production cross sections and studies of the need for 3-dimensional transport codes since angular deflections are more important than for heavy particles. However, the heavy ion problem is in much better shape with many of the remaining task ones of implementation. One exception may be further improvements in fragmentation cross sections and laboratory validation for the *Z=1* to *5* nuclei produced from the heavier projectile nuclei (Z>10). The present paper addressed two implementation tasks, the use of a free-space GCR model, which includes the isotopic composition of the primaries, and the extension of the HZETRN code to a full isotopic-grid. Because the use of a reduced-grid leads to error and there are no practical limitations in using the full isotopic-grid at this time, we recommend that the full isotopic-grid be used when initiatives to design space exploration vehicles begin. Future tasks that remain are to implement physical models (Webber, *et al.* 1990a) of the GCR isotopic environment and to continue to refine the QMSFRG model including comparisons to new fragmentation data as they become available. Such tasks are being considered by the present author and will be reported elsewhere.

## REFERENCES


Anonymous, Strategic Space Radiation Health Program Plan, NASA Office of Life Sciences and Microgravity Applications, Washington D.C. (1998).

G.D. Badhwar, and P.M O'Neill, An Improved Model of GCR for Space Exploration Missions. *Nucl. Tracks Radiat. Meas.* **20**, 403-410 (1992).

G.D. Badhwar and F.A. Cucinotta, A Comparison on Depth Dependence of Dose and Linear Energy Transfer Spectra in Aluminum and Polyethylene. *Radiation Research* **153**, 1-8 (2000).

C. Brechtmann, and W. Heinrich, Fragmentation Cross Sections of $^{32}S$ at 0.7, 1.2, and 200 GeV/nucleon, *Z.Phys.* **A331**, 463-472 (1988).

F.A. Cucinotta, Calculations of Cosmic-ray Helium Transport in Shielding Materials. NASA TP-3354 (1993).

F.A. Cucinotta, and R. R. Dubey, Alpha Cluster Description of Excitation Energies in $^{12}C$ ($^{12}C$, 3 $\alpha$) X at 2.1 GeV. *Physical Review C* **50**, 979-984 (1994).

F.A. Cucinotta, et al., Computational Procedures and Data-base Development. In: NASA Workshop on Shielding Strategies for Human Space Exploration. Eds. Wilson J.W,. Miller J., Konradi A., and Cucinotta F.A., NASA CP 3360 (1997).

F.A. Cucinotta, J.W. Wilson, J.L. Shinn, and R.K. Tripathi, Assessment and Requirements of Nuclear Reaction Data Bases for GCR Transport in the Atmosphere and Structures. *Adv. in Space. Res.* **21**, 1753-1762 (1998a).

F.A. Cucinotta, J.W. Wilson, R.K. Tripathi, and L.W. Townsend, Microscopic Fragmentation Model for Galactic Cosmic Ray Studies. *Advances in Space Research* **22**, 533-537 (1998b).

A. Hesse, *et al.*, The Isotopic Composition of Silicon and Iron in the Cosmic Radiation As Measured by the ALICE Experiment. 22$^{nd}$ International Conference, The Dublin Institute for Advanced Studies, Dublin, 596-599 (1991).

M. Kim, J.W. Wilson, R.L. Kiefer, and S.A. Thibeault, Effects of Isotope Selection on Solution Convergence in HZE Transport. NASA TP 3445 (1994).

C.N. Knott, *et al.,* Interactions of Relativistic Neon to Nickel Projectiles in Hydrogen, Elemental Production Cross Sections. *Physical Review C.* **53**, 347-357 (1996).

C.N. Knott, *et al.,* Interactions of Relativistic $^{36}Ar$ and $^{40}Ar$ Nuclei in Hydrogen: Isotopic Production Cross Sections. *Physical Review C* **56**, 398-406 (1997).

J. Letaw, C.H. Tsao, and R. Silberberg, Matrix Methods of Cosmic Ray Propagation. Composition and Origin of Cosmic Rays, Maurice M. Shapiro, ed., D. Reidel Publ. Co, 337-342 (1983).

A. Lukasiak, P. Ferrando, F.B. McDonald, and W.R. Webber, Cosmic Ray Composition of 6<Z<8 Nuclei in the Energy Range 50-150 MeV/n by the Voyager Spacecraft During the Solar Minimum and Maximum Periods. 23rd International Cosmic Ray Conference, La Jolla , USA, 539-542 (1993).

E.N. Parker, The Passage of Energetic Particles Through Interplanetary Space. *Planet Space Sci.* **13**, 9-49 (1965).

W. Schimmerling, J. Miller, M. Wong, M. Rapkin, J. Howard, H.G. Spieler, and Blair, J.V., The Fragmentation of 670A MeV Neon-20 as a Function of Depth in Water. *Radiation Research* **120**, 36-51 (1989).

J.L. Shinn, J.W. Wilson, F.F. Badavi, Fully-Energy Dependent HZETRN. NASA TP (1994).

L.W. Townsend, J.W. Wilson, F.A. Cucinotta, and J.W. Norbury, Comparison of Optical Model Differences in Heavy Ion Fragmentation: Optical Versus Geometric. *Physical Review C,* **34**, 1491-1495 (1986).

W.R. Webber, J.C. Kish, and D.A. Schrier, Cosmic Ray Isotope Measurements with a New Cerenkov x Total Energy Telescope. 19th International Cosmic Ray Conference, La Jolla , USA, 88-95 (1985).

W.R. Webber, A. Southoul, P. Ferrando, and M. Gupta, The Source Charge and Isotropic Abundances of Cosmic Rays with Z=9-16: A Study Using New Fragmentation Cross-Sections. *The Astrophys. J.* **348**, 611-620 (1990a).

W.R. Webber, J.C. Kih, and D.A. Schrier, *Phys. Rev. C **41***, 547 (1990b).

M.E. Wiedenback and D.E. Greiner, High-Resolution Observations of the Isotopic Composition of Carbon And Silicon in the Galactic Cosmic Rays. *The Astrophys. J.* **247** L119-L122 (1981).

M.E. Wiedenback, The Isotopic Composition on Cosmic Ray Chlorine, 19th International Cosmic Ray Conference, La Jolla , USA, 1985, 84-87 (1985).

J.W. Wilson, L.W. Townsend, W. Schimmerling, G.S. Khandelwal, F. Khan, J.E. Nealy, F.A. Cucinotta, L.C. Simonsen, J.L. Shinn, and J.W. Norbury, Transport Methods and Interactions for Space Radiations. NASA RP 1257 (1991).

J.W. Wilson, S.A. Thibeault, J.E. Nealy, M.Y. Kim, and R.L. Kiefer, Studies in Space Radiation Shield Performance. Proceedings of the Engineering & Architecture Symposium, Prairie View A&M Univ., 169-176 (1993).

J.W. Wilson, *et al.,* NUCFRG2: An Evaluation of the Semiempirical Nuclear Fragmentation Database. NASA TP 3533 (1995).

C. Zeitlin, L. Heilbronn, J. Miller, S.E. Rademacher, T. Borak, T.R. Carter, K.A. Frankel, W. Schimmerling, and C.E. Stronach, Heavy Fragment Production Cross Sections from 1.05 GeV/nucleon $^{56}$Fe in C, Al, Cu, Pb, and $CH_2$ Target. *Physical Review C* **56**, 388-3397 (1997).

C. Zeitlin, A. Fukumura, L. Heilbronn, Y. Iwata, J. Miller, T. Murakami, Fragmentation Cross Sections of 600 MeV/nucleon $^{20}$Ne on Elemental Targets. *Physical Review C* **64**, 24902 (2001).

C. Zeitlin, L. Heilbronn, J. Miller, A. Fukumura, Y. Iwata, and T. Murakami, Charge-changing and fragment production cross sections of $^{28}$Si on elemental targets from 400 MeV/nucleon to 1200 MeV/nucleon, LBNL-47655 (2002).

**Figure Captions**

Fig. 1. Parametric model for describing the change in isotopic composition versus the solar modulation parameter, $\phi(MV)$.

Fig. 2. Comparisons of the QMSFRG model to experiment for the elemental distribution of fragments from $^{20}$Ne on $^{12}$C interactions at 0.6 GeV/u. Experimental data from Zeitlin et al. (2001).

Fig. 3. Comparisons of the QMSFRG model to experiment for the elemental distribution of fragments from $^{22}$Ne on $^{1}$H interactions at 0.894 GeV/u. Experimental data from Knott et al. (1996).

Fig. 4. Comparisons of the QMSFRG model to experiment for the elemental distribution of fragments from $^{26}$Mg on $^{1}$H interactions at 0.576 GeV/u. Experimental data from Knott et al. (1996).

Fig. 5. Comparisons of the QMSFRG model to experiment for the elemental distribution of fragments from $^{28}$Si on $^{12}$C interactions at 0.6 GeV/u. Experimental data from Zeitlin et al. (2002).

Fig. 6. Comparisons of the QMSFRG model to experiment for the elemental distribution of fragments from $^{32}$S on $^{27}$Al interactions at 1.2 GeV/u. Experimental data from Brechtmann and Heinrich (1988).

Fig. 7. Comparisons of the QMSFRG model to experiment for the elemental distribution of fragments from $^{36}$Ar on $^{1}$H interactions at 0.765 GeV/u. Experimental data from Knott et al. (1996).

Fig. 8. Comparisons of the QMSFRG model to experiment for the elemental distribution of fragments from $^{40}$Ar on $^{1}$H interactions at 0.352 GeV/u. Experimental data from Knott et al. (1996).

Fig. 9. Comparisons of the QMSFRG model to experiment for the elemental distribution of fragments from $^{40}$Ca on $^{12}$C interactions at 0.763 GeV/u. Experimental data from Knott et al. (1996).

Fig. 10. Comparisons of the QMSFRG model to experiment for the isotopic distribution of fragments from $^{40}$Ar on $^{12}$C interactions at 0.6 GeV/u. Experimental data from Webber et al. (1990b).

Fig. 11. Comparisons of the QMSFRG model to experiment for the elemental distribution of fragments from $^{56}$Fe on $^{12}$C interactions at 0.6 GeV/u. Experimental data from Webber et al. (1990b).

Fig. 12. Comparisons of results from the HZETRN Code for the mass flux distribution behind 5 g/cm$^2$ of aluminum shielding for solar minimum conditions comparing transport with a reduced 59-isotope grid to transport with a full 141-isotope grid.

Fig. 13. Comparisons of the error that results from the HZETRN Code for the mass flux distribution near solar minimum when using a reduced 59-isotope grid compared to transport with a full 141-isotope grid.

Fig. 14. Comparisons of the error that results from the HZETRN Code for the elemental flux distribution near solar minimum when using a reduced 59-isotope grid compared to transport with a full 141-isotope grid.

Fig. 15. Comparisons of the error that results from the HZETRN Code for the mass flux distribution near solar maximum when using a reduced 59-isotope grid compared to transport with a full 141-isotope grid.

Fig. 16. Comparisons of the error that results from the HZETRN Code for the elemental flux distribution near solar maximum when using a reduced 59-isotope grid compared to transport with a full 141-isotope grid.

**Table 1a.** Isotopic Composition of GCR Elements Z=5-13.

| *Isotope* | *Near-Earth Fraction* | *Source Fraction* |
|---|---|---|
| | Z=5 | |
| $^{10}B$ | 0.31 | 0.2 |
| $^{11}B$ | 0.69 | 0.8 |
| | Z=6 | |
| $^{12}C$ | 0.924 | 0.999 |
| $^{13}C$ | 0.076 | 0.001 |
| | Z=7 | |
| $^{14}N$ | 0.427 | 0.782 |
| $^{15}N$ | 0.573 | 0.218 |
| | Z=8 | |
| $^{16}O$ | 0.946 | 0.985 |
| $^{17}O$ | 0.0274 | 0.008 |
| $^{18}O$ | 0.0265 | 0.007 |
| | Z=10 | |
| $^{20}Ne$ | 0.547 | 0.681 |
| $^{21}Ne$ | 0.106 | 0.0 |
| $^{22}Ne$ | 0.347 | 0.319 |
| | Z=12 | |
| $^{24}Mg$ | 0.648 | 0.736 |
| $^{25}Mg$ | 0.175 | 0.136 |
| $^{26}Mg$ | 0.177 | 0.128 |
| | Z=13 | |
| $^{26}Al$ | 0.02 | 0.0 |
| $^{27}Al$ | 0.98 | 1.0 |

**Table 1b.** Isotopic Composition of GCR Elements Z=14-26.

| *Isotope* | *Near-Earth Fraction* | *Source Fraction* |
|---|---|---|
| | Z=14 | |
| $^{28}$Si | 0.840 | 0.902 |
| $^{29}$Si | 0.081 | 0.054 |
| $^{30}$Si | 0.079 | 0.044 |
| | Z=16 | |
| $^{32}$S | 0.698 | 0.962 |
| $^{33}$S | 0.145 | 0.019 |
| $^{34}$S | 0.157 | 0.019 |
| | Z=17 | |
| $^{35}$Cl | 0.523 | 1.0 |
| $^{36}$Cl | 0.414 | 0.0 |
| $^{37}$Cl | 0.261 | 0.0 |
| | Z=18 | |
| $^{36}$Ar | 0.637 | 1.0 |
| $^{37}$Ar | 0.314 | 0.0 |
| $^{38}$Ar | 0.026 | 0.0 |
| $^{40}$Ar | 0.026 | 0.0 |
| | Z=20 | |
| $^{40}$Ca | 0.4 | 1.0 |
| $^{41}$Ca | 0.2 | 0.0 |
| $^{42}$Ca | 0.2 | 0.0 |
| $^{43}$Ca | 0.2 | 0.0 |
| $^{44}$Ca | 0.2 | 0.0 |
| | Z=26 | |
| $^{54}$Fe | 0.076 | 0.055 |
| $^{55}$Fe | 0.084 | 0.078 |
| $^{56}$Fe | 0.763 | 0.792 |
| $^{57}$Fe | 0.076 | 0.075 |

Figure 1.

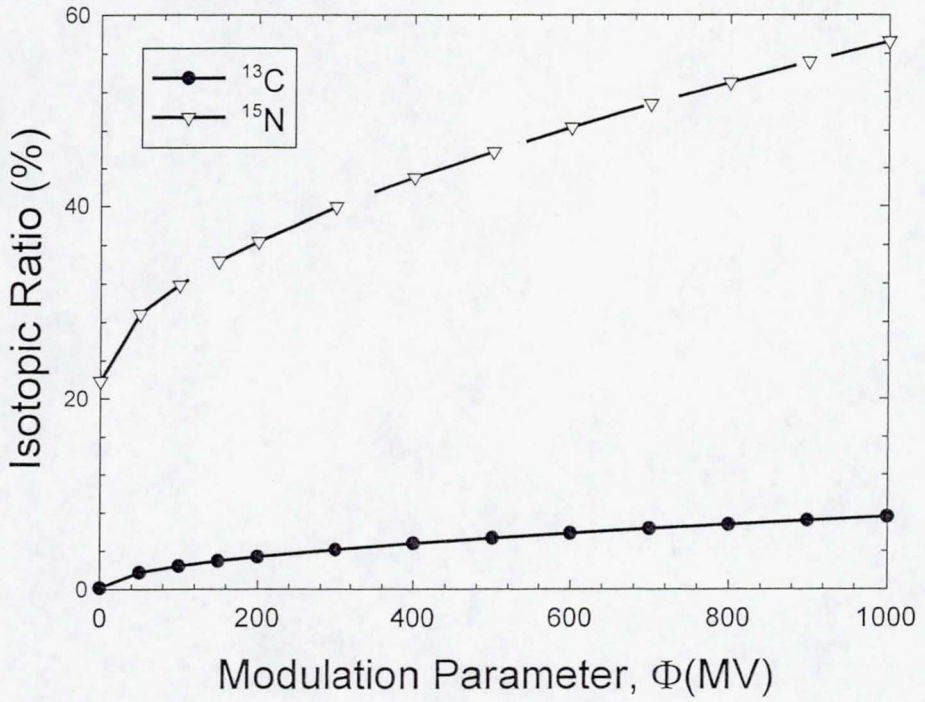
60
40
20
0
0
200
400
600
800
1000
Isotopic Ratio (%)
Modulation Parameter, Φ(MV)
$^{13}C$
$^{15}N$

Figure 2.

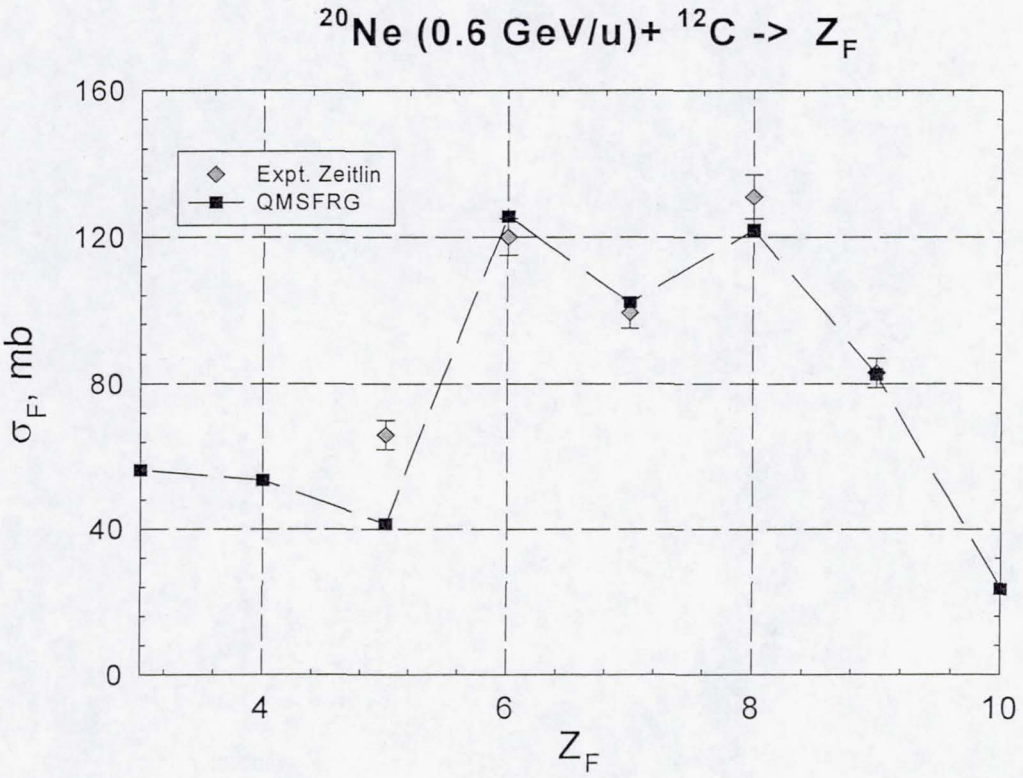
$^{20}$Ne (0.6 GeV/u)+ $^{12}$C -> $Z_F$
Expt. Zeitlin
QMSFRG
$\sigma_F$, mb
160
120
80
40
0
4
6
8
10
$Z_F$

Figure 3.

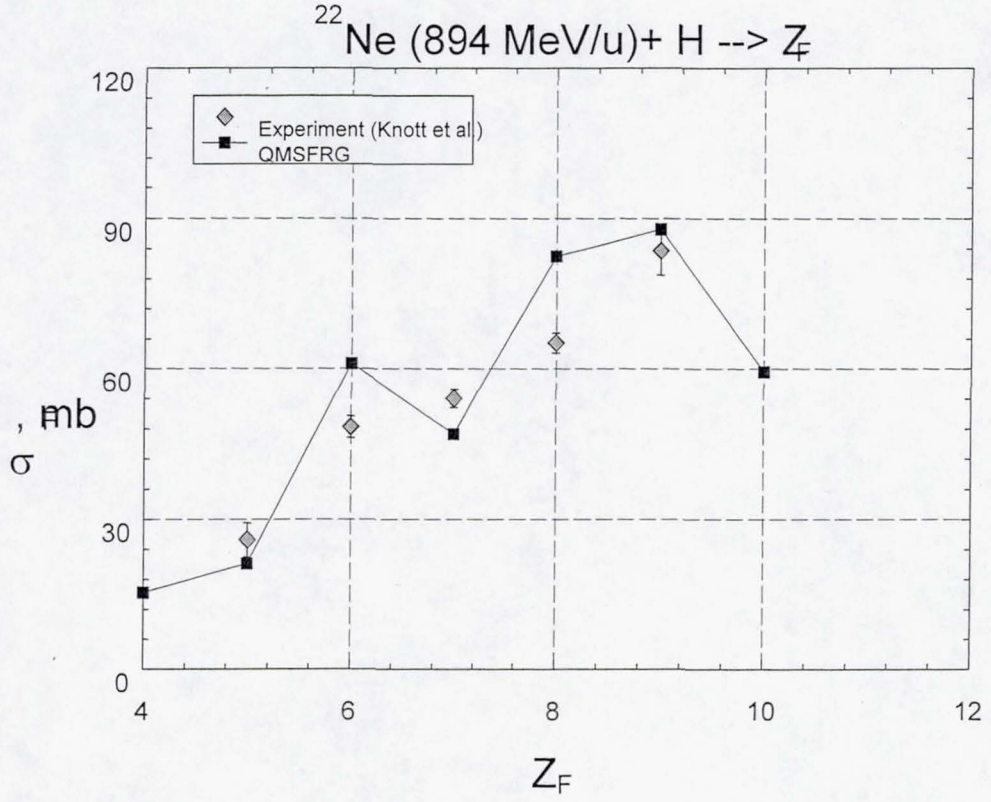
22Ne (894 MeV/u)+ H --> ZF
Experiment (Knott et al.)
QMSFRG
120
90
60
30
0
σ, mb
4
6
8
10
12
ZF

Figure 4.

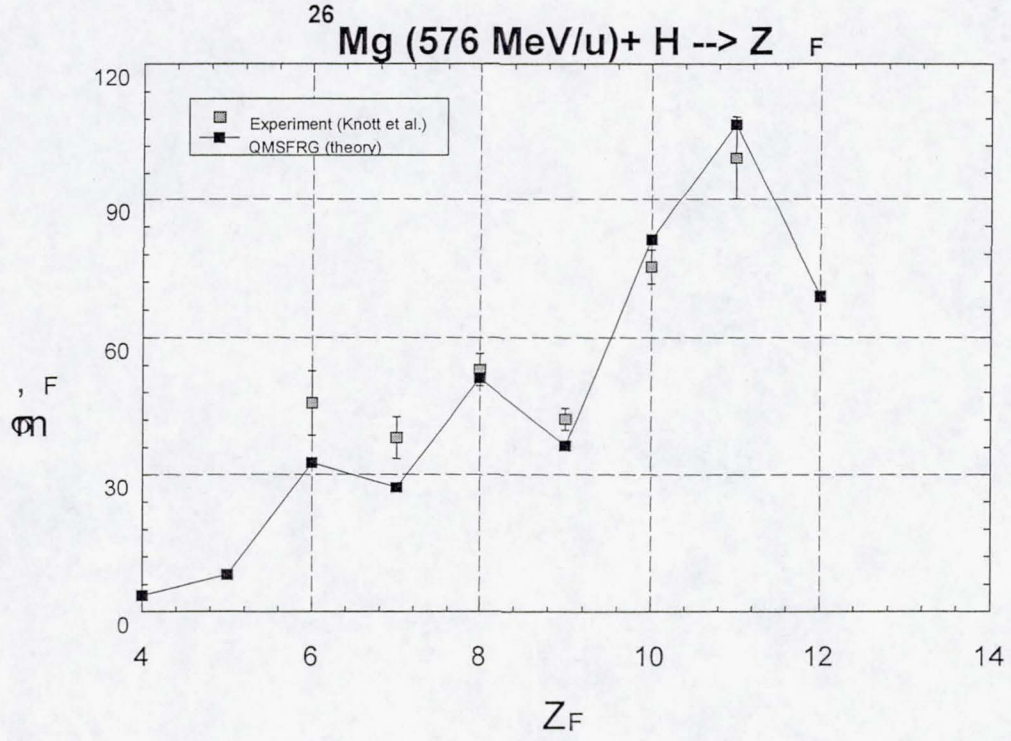
26
Mg (576 MeV/u)+ H --> Z F
Experiment (Knott et al.)
QMSFRG (theory)
120
90
60
30
0
4
6
8
10
12
14
ZF

Figure 5.

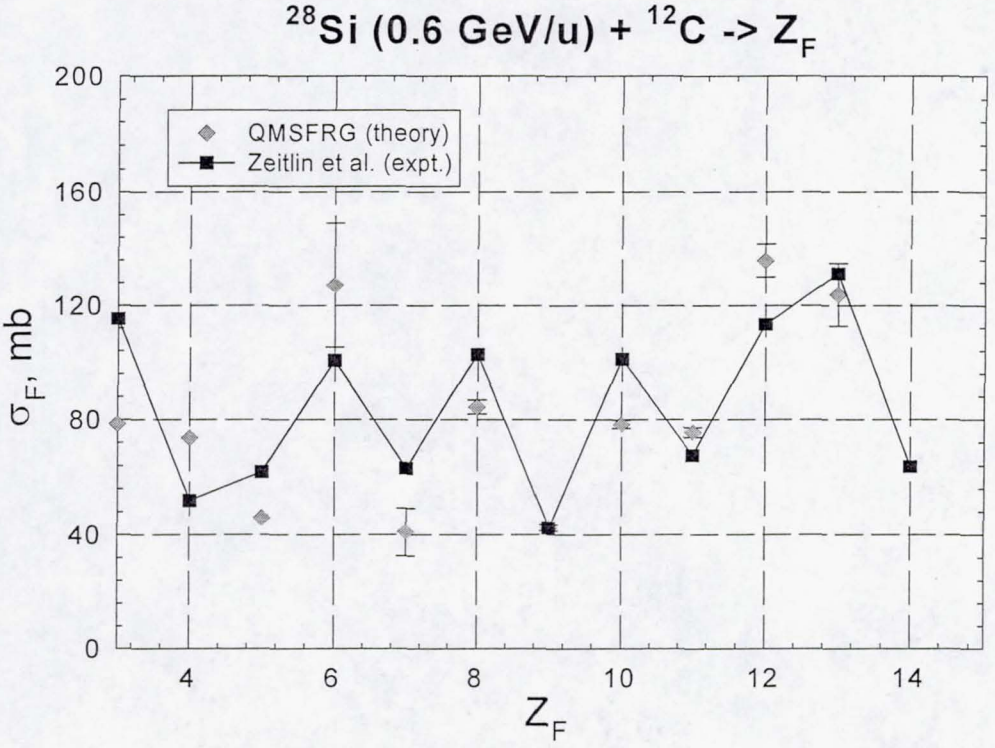
$^{28}$Si (0.6 GeV/u) + $^{12}$C -> $Z_F$
QMSFRG (theory)
Zeitlin et al. (expt.)
$\sigma_F$, mb
$Z_F$
0
40
80
120
160
200
4
6
8
10
12
14

Figure 6.

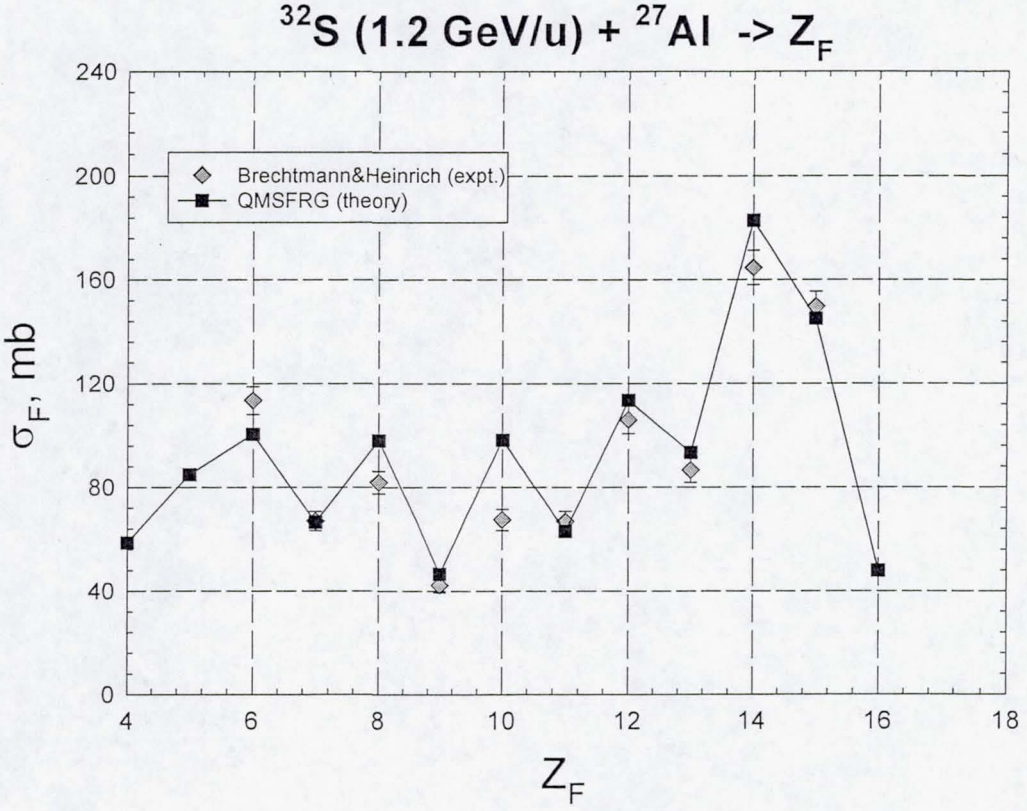
$^{32}$S (1.2 GeV/u) + $^{27}$Al -> $Z_F$
Brechtmann&Heinrich (expt.)
QMSFRG (theory)
$\sigma_F$, mb
$Z_F$
0
40
80
120
160
200
240
4
6
8
10
12
14
16
18

Figure 7.

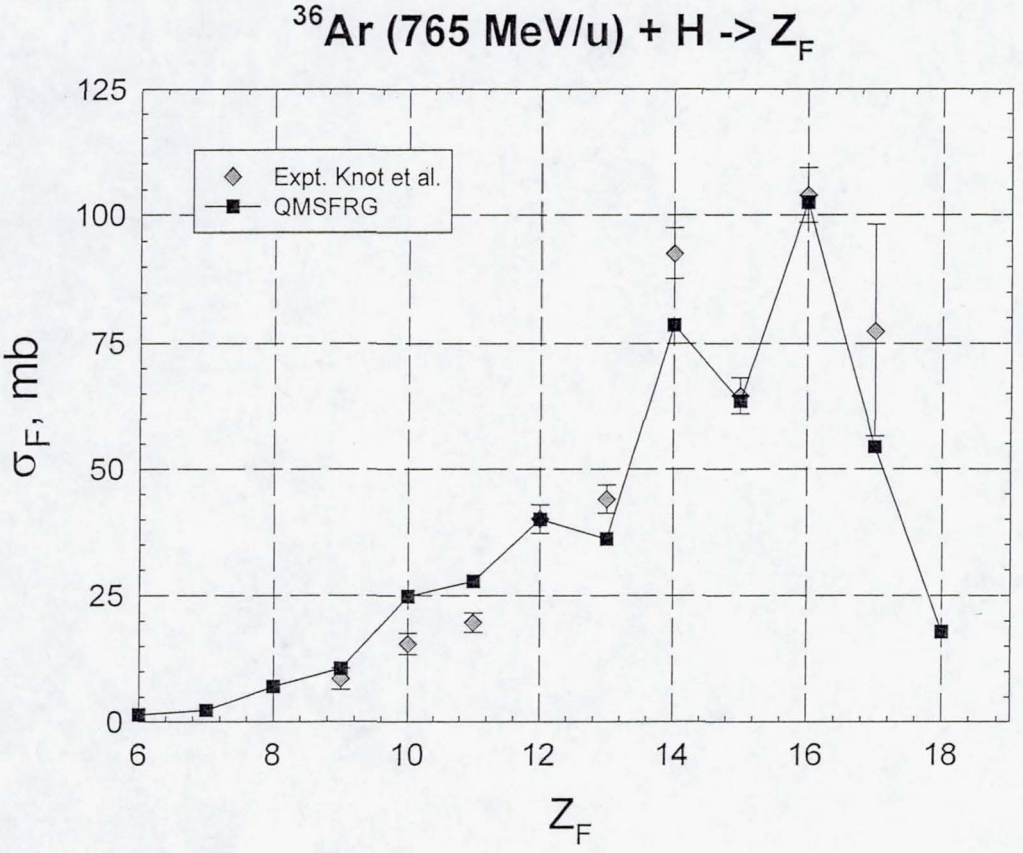
$^{36}$Ar (765 MeV/u) + H -> $Z_F$
Expt. Knot et al.
QMSFRG
$\sigma_F$, mb
$Z_F$
0
25
50
75
100
125
6
8
10
12
14
16
18

Figure 8.

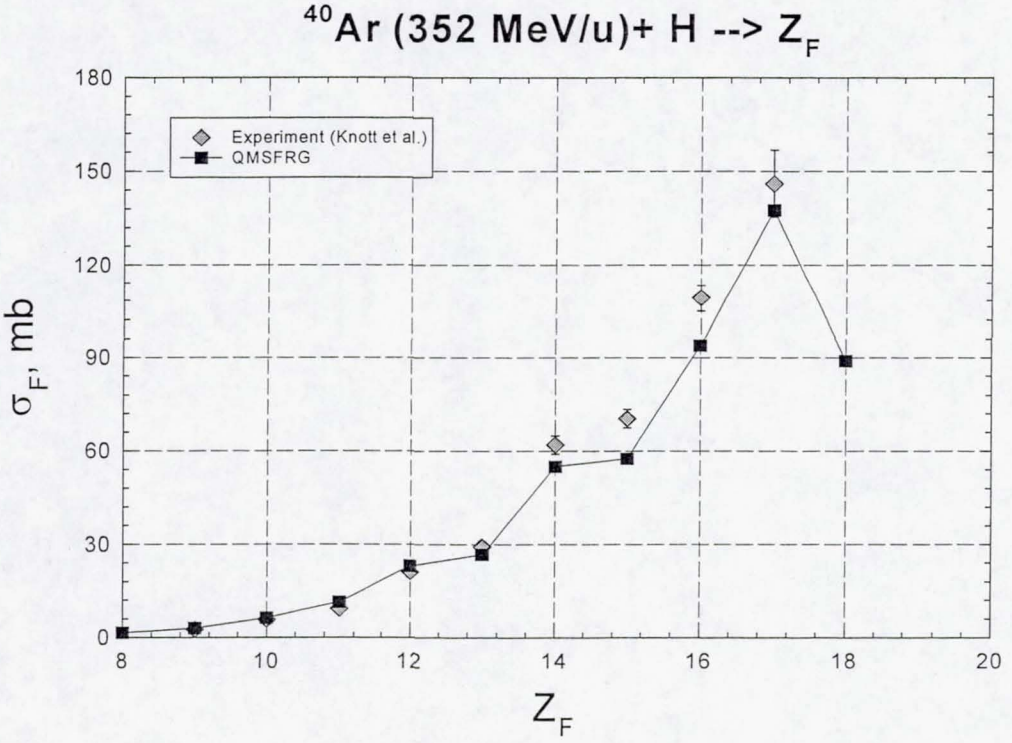
$^{40}$Ar (352 MeV/u)+ H --> $Z_F$
Experiment (Knott et al.)
QMSFRG
$\sigma_F$, mb
$Z_F$
0
30
60
90
120
150
180
8
10
12
14
16
18
20

Figure 9.

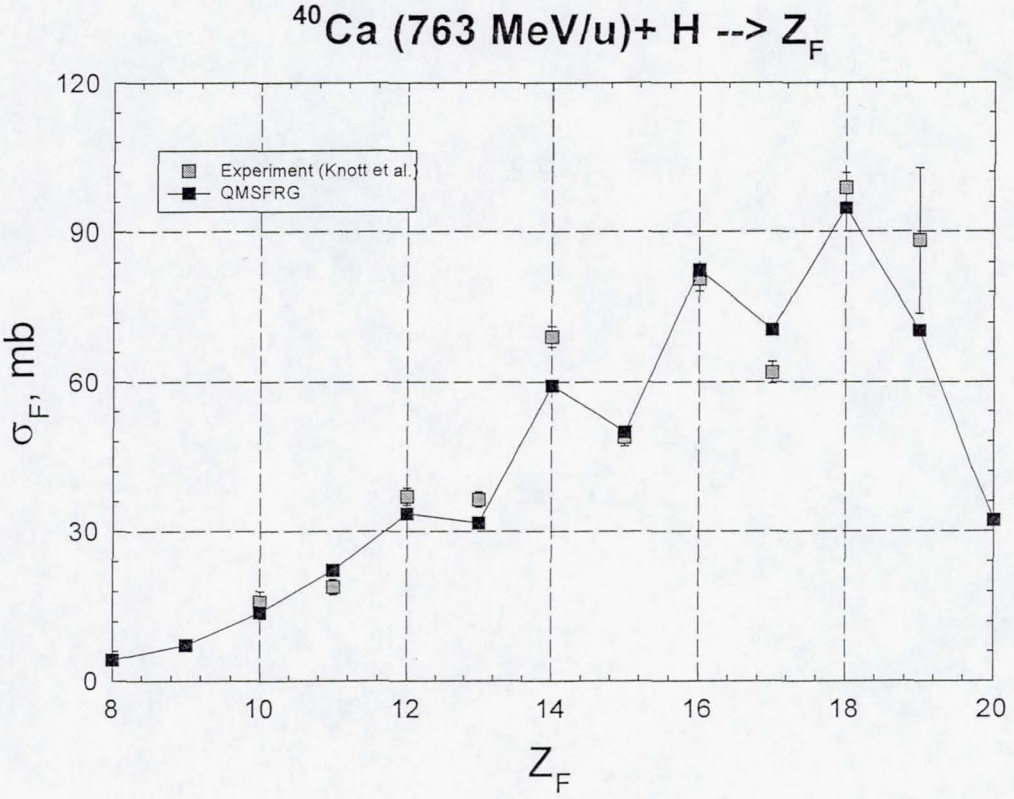
$^{40}$Ca (763 MeV/u)+ H --> $Z_F$
Experiment (Knott et al.)
QMSFRG
$\sigma_F$, mb
$Z_F$
0
30
60
90
120
8
10
12
14
16
18
20

Figure 10.

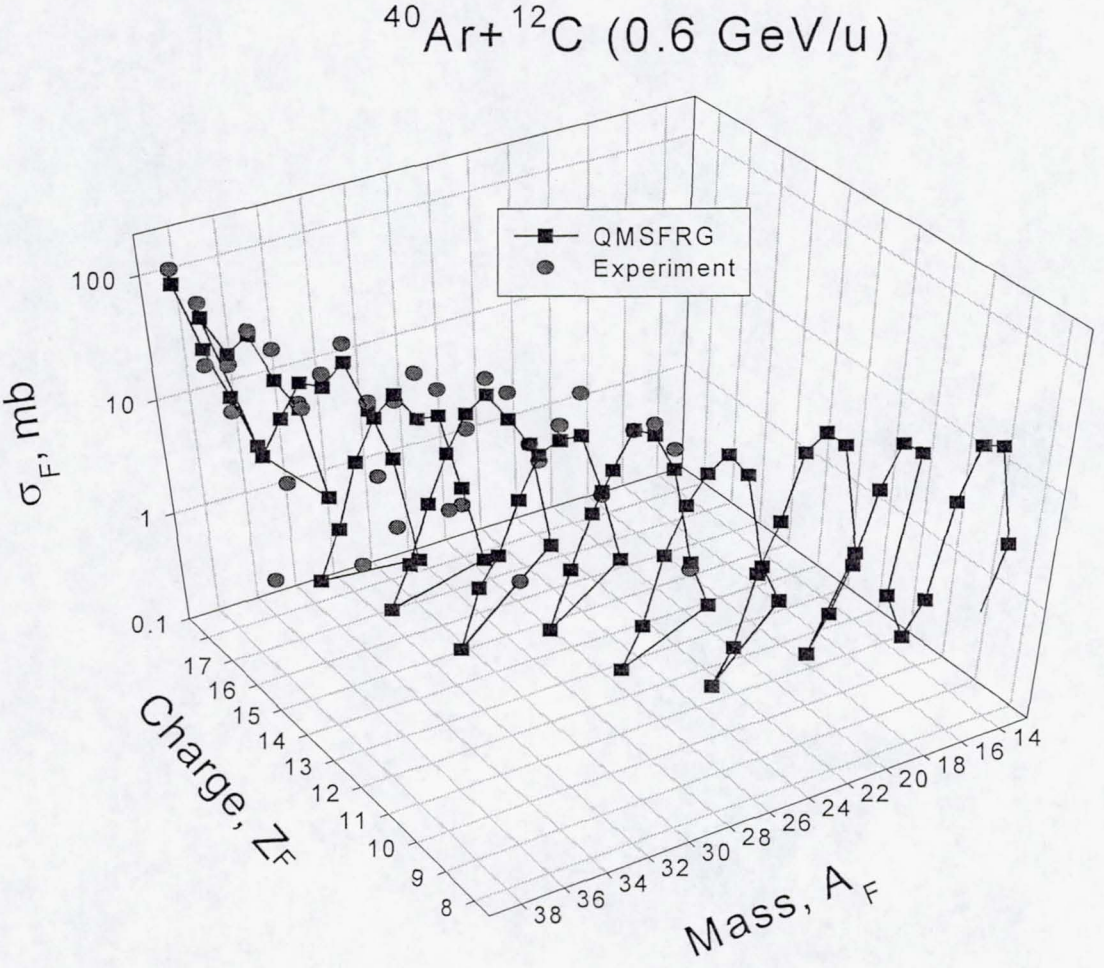
$^{40}$Ar+$^{12}$C (0.6 GeV/u)
QMSFRG
Experiment
$\sigma_F$, mb
100
10
1
0.1
Charge, $Z_F$
17
16
15
14
13
12
11
10
9
8
Mass, $A_F$
38
36
34
32
30
28
26
24
22
20
18
16
14

Figure 11.

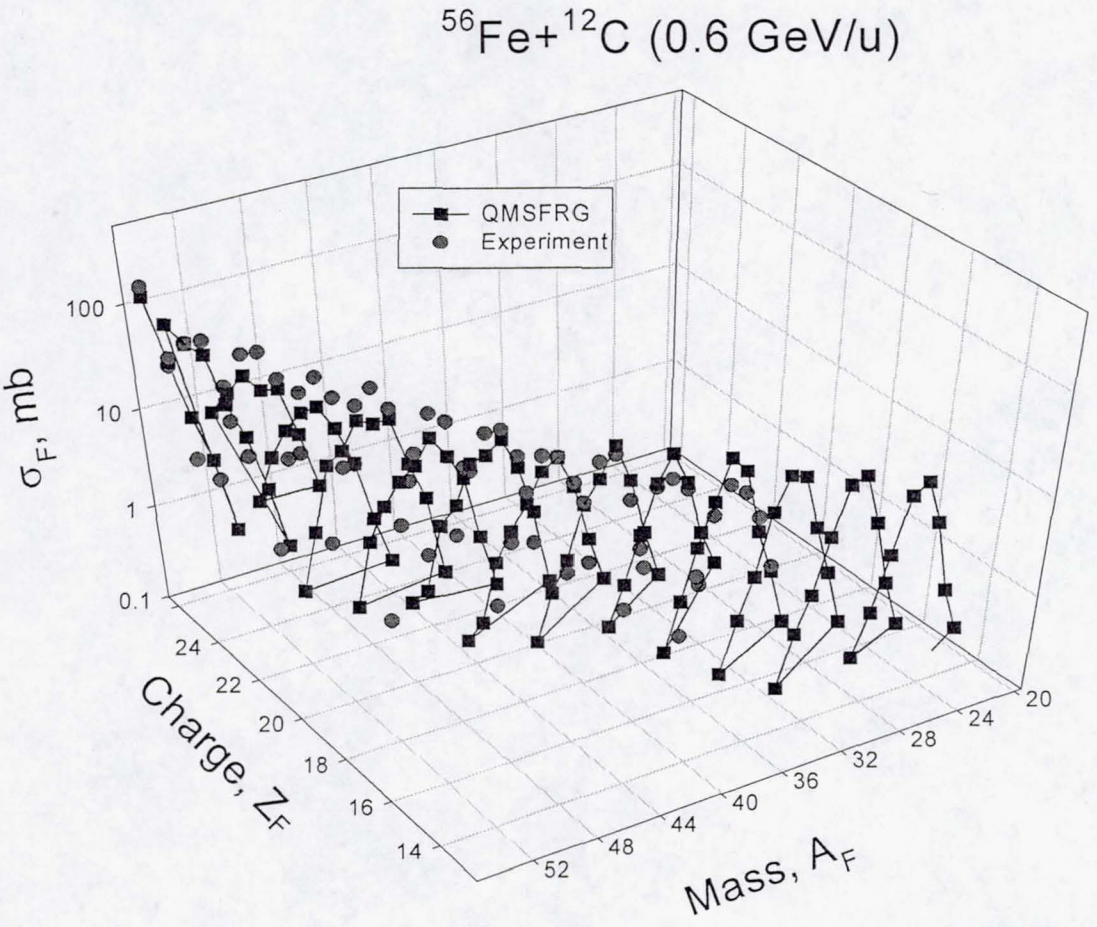
$^{56}Fe+^{12}C$ (0.6 GeV/u)
QMSFRG
Experiment
$\sigma_F$, mb
100
10
1
0.1
Charge, $Z_F$
24
22
20
18
16
14
Mass, $A_F$
52
48
44
40
36
32
28
24
20

Figure 12.

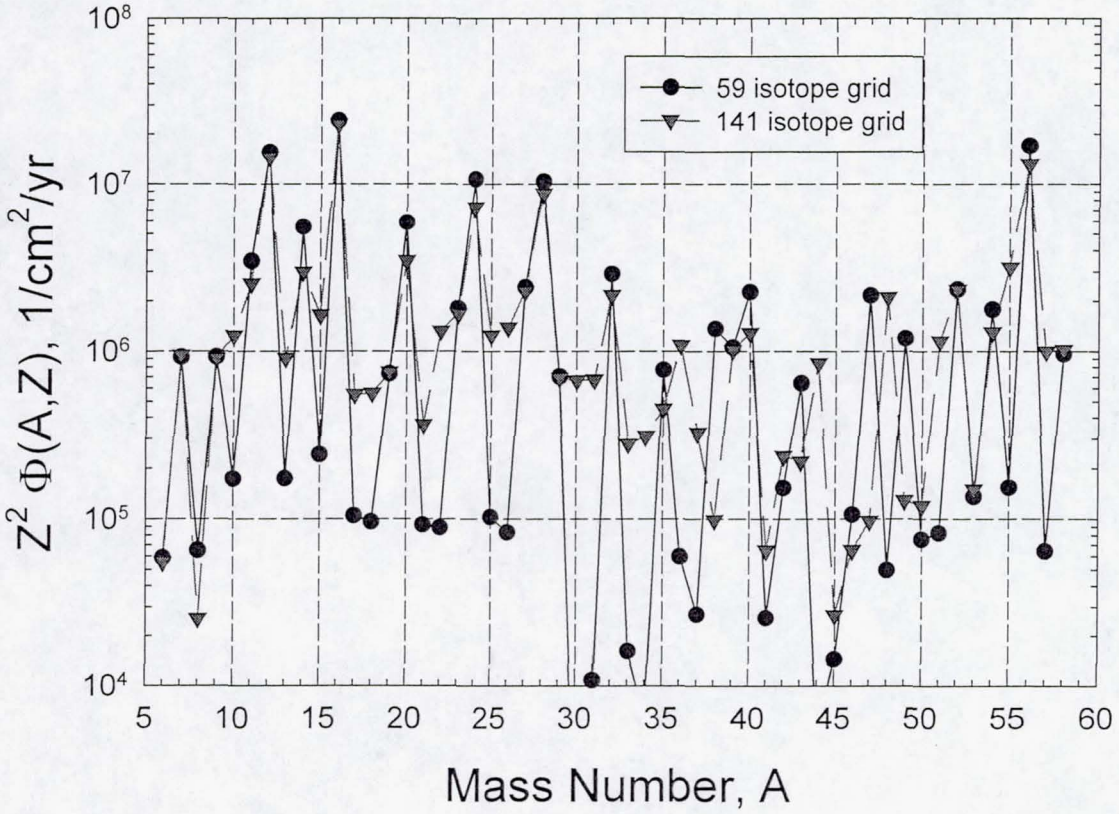
59 isotope grid
141 isotope grid
$Z^2\,\Phi(A,Z)$, 1/cm$^2$/yr
$10^8$
$10^7$
$10^6$
$10^5$
$10^4$
5
10
15
20
25
30
35
40
45
50
55
60
Mass Number, A

Figure 13.

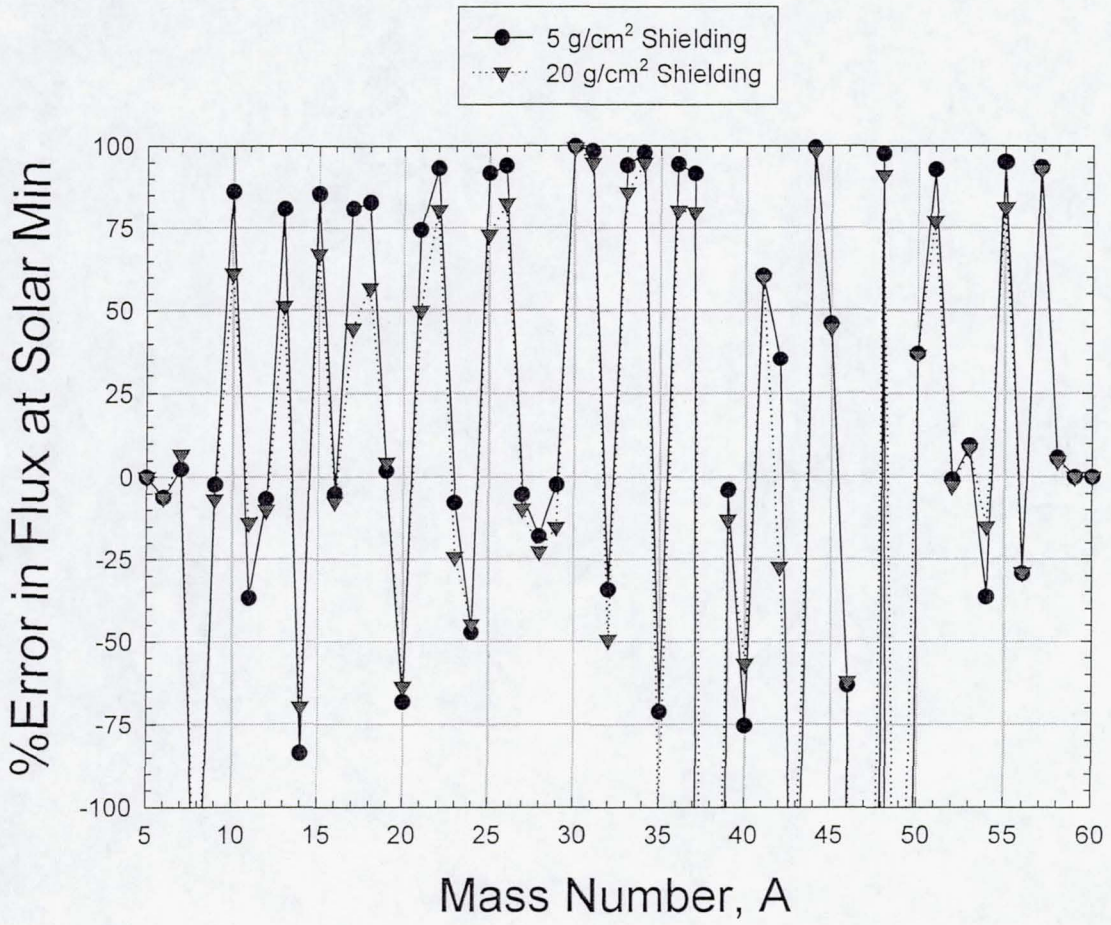
5 g/cm2 Shielding
20 g/cm2 Shielding
%Error in Flux at Solar Min
100
75
50
25
0
-25
-50
-75
-100
5
10
15
20
25
30
35
40
45
50
55
60
Mass Number, A

Figure 14.

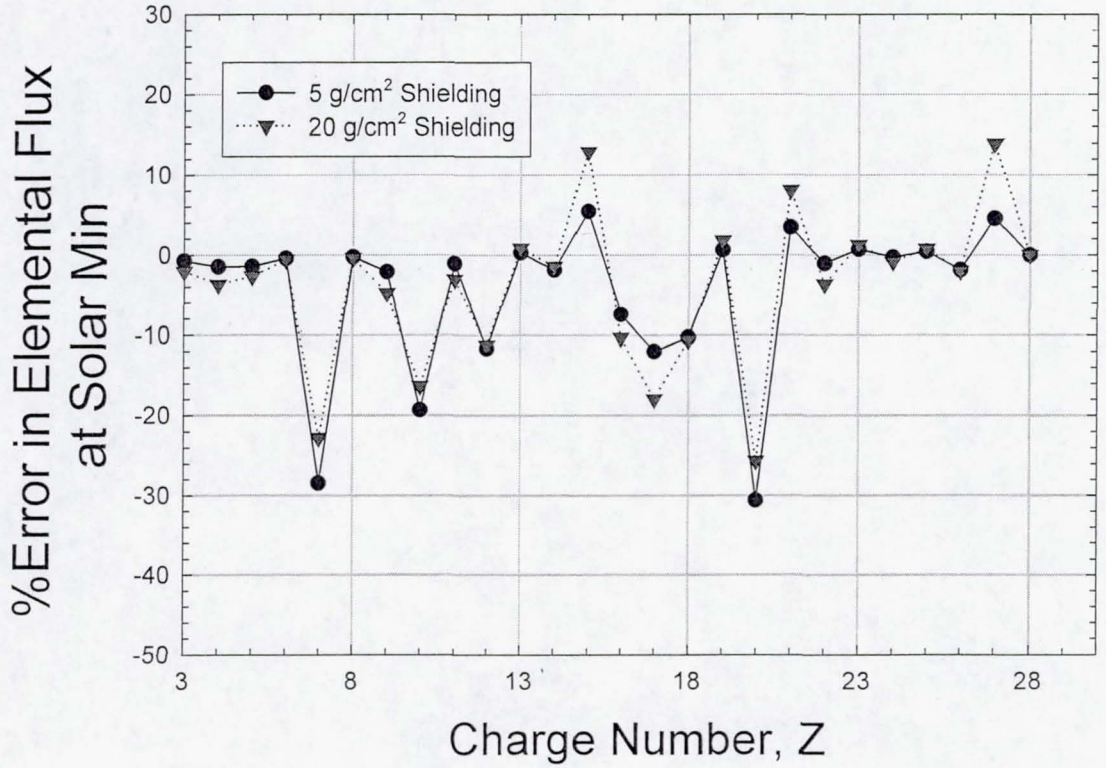
%Error in Elemental Flux at Solar Min
5 g/cm$^2$ Shielding
20 g/cm$^2$ Shielding
30
20
10
0
-10
-20
-30
-40
-50
3
8
13
18
23
28
Charge Number, Z

Figure 15.

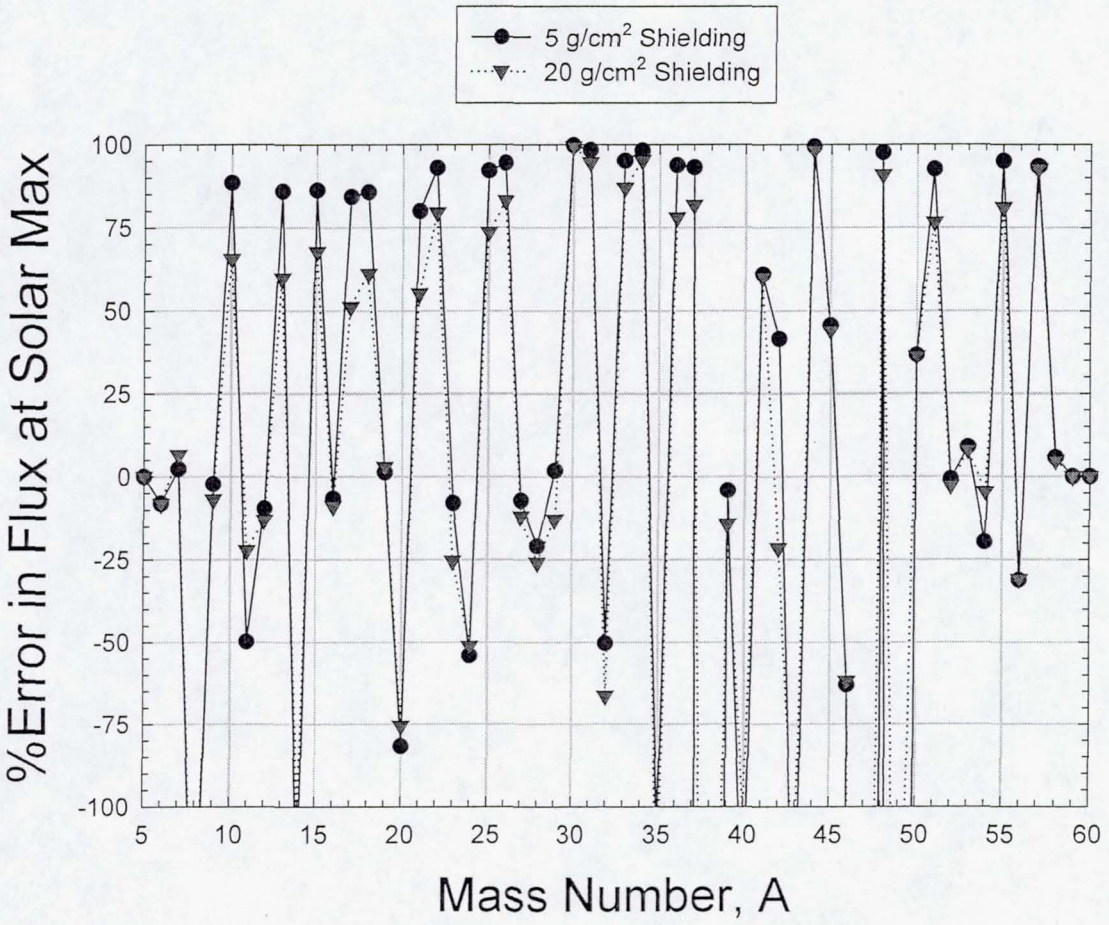
5 g/cm2 Shielding
20 g/cm2 Shielding
%Error in Flux at Solar Max
100
75
50
25
0
-25
-50
-75
-100
5
10
15
20
25
30
35
40
45
50
55
60
Mass Number, A

Figure 16.

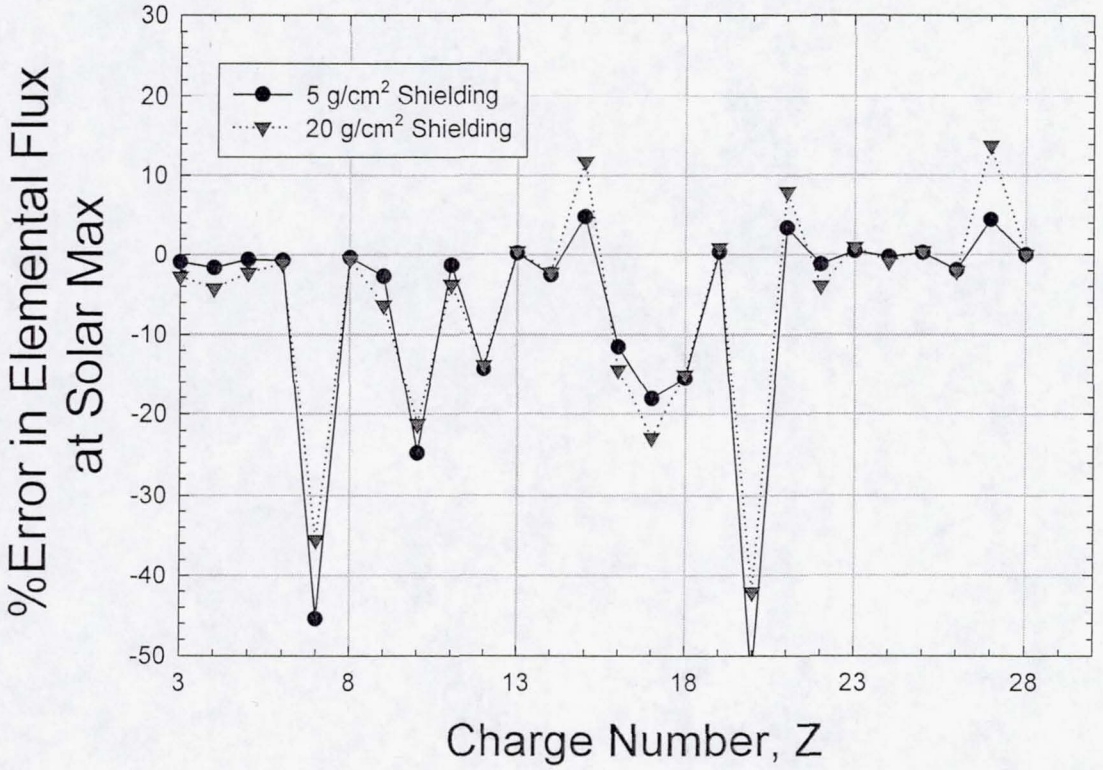
%Error in Elemental Flux at Solar Max
5 g/cm$^2$ Shielding
20 g/cm$^2$ Shielding
30
20
10
0
-10
-20
-30
-40
-50
3
8
13
18
23
28
Charge Number, Z